1995

Flow over mountains: Coriolis force, transient troughs and three dimensionality

Peng, Melinda S.

Q. J. R. Meteorol. Soc. (1995), Volume 121, pp. 593-613
http://hdl.handle.net/10945/44176

Q. J. R. Meteorol. Soc. (1995), **121**, pp. 593–613 551.558.21

Flow over mountains: Coriolis force, transient troughs and three dimensionality

By MELINDA S. PENG[1]*, SHANG-WU LI[1]†, SIMON W. CHANG[2] and R. T. WILLIAMS[1]

[1] *Naval Postgraduate School, Monterey, USA*
[2] *Naval Research Laboratory, Monterey, USA*

(Received 7 January 1994; revised 31 October 1994)

SUMMARY

Some issues, concerning uniform, stratified flow over a three-dimensional mountain, that have not been fully explored are studied using primitive-equation models. When the Froude number (Fr) is small (e.g. $Fr < 0.5$), we find that the Coriolis force cannot be neglected for flow over small-scale mountains (characteristic length $L < 50$ km) even though the Rossby number (Ro) is large. When the Coriolis force is neglected, a pair of symmetric vortices is induced on the lee side, irrespective of the scale of the mountain, as long as Fr lies roughly between 0.1 and 0.5. The major effect of the Coriolis force is to modify or diminish the lee vortices due to the leftward deflection on the upstream side of the mountain. The Coriolis deflection also reduces the upstream propagation. When Fr is ≥ 1, most of the flow goes over the mountain and the Coriolis effect is small for the same Ro. Therefore, the importance of the Coriolis effect is determined by both Ro and Fr.

As the scale of the mountain increases from small-scale to mesoscale (100 km $< L <$ 300 km), the upstream flow is deflected more to the left by the Coriolis effect, and a trough develops on the lee side. The length-scale of the trough depends on the scale of the mountain in the along-flow direction. For smaller-scale mountains, small vortices can be generated within the lee-side trough when Fr is small. When the mountain scale is increased, the lee-side vortices disappear, and only a lee-side trough remains. Depending on the mean wind speed and the mountain scale, the lee-side trough can be advected by the anticyclonic flow over the mountain to the south, and remain attached to the mountain for a long time. A train of troughs is generated on the lee side of an elliptic mountain associated with the lee-side gravity waves.

Simulations of flows over mountains in two-dimensional and three-dimensional models with the same cross-sectional profile are compared. For small-scale mountains ($L < 100$ km), the two-dimensional model overestimates the amount of airflow over the mountain and also the lee-side downslope wind.

1. INTRODUCTION

It is well known that atmospheric motions of various scales are significantly influenced by the presence of mountains. Due to the very broad spectrum of mountain scales, ranging from tens to thousands of kilometres, various theoretical and numerical studies are usually devoted to a mountain with a particular scale, or to a particular type of phenomenon that is related to the mountain. A general review on this topic is given by Smith (1979b). In a more recent review Smith (1989) concentrates on lee-side gravity waves, flow splitting, and wave breaking, while Durran (1990) focuses mainly on the gravity waves and the downslope wind. The purpose of this study is to address some of the more subtle points on flows over mountains. We hope to link together solutions obtained for different scales of mountains to obtain a general picture of stratified, barotropic flows over mountains. The major parameters determining the characteristics of uniform stratified flow over topography are the Rossby number ($Ro = U/fL$) and the Froude number ($Fr = U/Nh$), where U is the characteristic speed, L is the horizontal scale of the mountain, f is the Coriolis parameter, N is the Brunt–Väisälä frequency related to the stratification of the fluid, and h is the maximum mountain height. One of our main objectives is to determine whether the flow goes around or over a mountain for different mountain sizes (horizontal scale), shapes, heights and mean wind speeds. We intend to: (i) study the effect of the Coriolis force for flows over small-scale mountains; (ii) study the change in character of the flow over mesoscale to synoptic-scale mountains;

* Corresponding author: Department of Meteorology, Naval Postgraduate School, Monterey, California 93943-5100, USA.
† Now affiliated with the Central Weather Bureau, Taipei, Taiwan.

(iii) study flows over large-scale mountains, and (iv) compare the flow over an infinite ridge with flow over a three-dimensional (3D) mountain with the same cross-sectional profile.

In this study we employ both two-dimensional (2D) and 3D hydrostatic primitive-equation models. The numerical experiments are selected so that a general picture of the flow for various parametric values can be obtained. This study is limited to uniform, barotropic flow over topography in a uniformly stratified fluid. Some differences that may arise from non-uniform flows will be reported in a separate paper. This paper is organized as follows. The 2D and 3D numerical models used are described briefly in section 2. The effect of the Coriolis force for flow over mountains with small horizontal scales is examined in section 3. The general flow patterns for mountains ranging from mesoscale to synoptic scale are presented in section 4, and section 5 is devoted to flow over large-scale mountains. Comparisons between the 2D flow and 3D flow with the same mountain cross-sectional profile are discussed in section 6. The results are summarized in section 7.

2. Description of numerical models and topography

(*a*) *The 2D numerical model*

The 2D numerical model, which uses the hydrostatic Boussinesq equations, is described in detail by Williams *et al.* (1992). There are 36 levels in the vertical, and the horizontal grid interval equals 5 and 40 km, respectively, for the two experiments discussed in section 6. Periodic boundary conditions are used in the east–west direction. A rigid-lid boundary is applied at the top, with increased diffusion coefficients in the upper one third of the domain to control reflection from the upper boundary. The main use of this model is to compare infinite ridge solutions with solutions for a finite mountain with the same cross-sectional mountain profile.

(*b*) *The 3D numerical model*

The 3D model is a modified version of the Naval Research Laboratory limited-area numerical model (Madala *et al.* 1987) on an f-plane. This hydrostatic primitive-equation model uses second-order finite differences and a split-explicit time integration scheme for handling the gravity waves. The horizontal grid of the model is arranged on the Arakawa staggered C-grid. The model employs the terrain-following σ vertical coordinate (where σ is the ratio of the pressure to the surface pressure). For the present study, the parametrized physics of the model is turned off except for the dry convective adjustment and the horizontal diffusion. For all experiments there are 16 levels in the vertical, except that 36 levels are used in comparison with the 2D model. The horizontal grid interval ranges from 5 km to 160 km, in proportion to the horizontal mountain scale. In each experiment the grid size is one fifth of the mountain scale a_{ox} defined in the following subsection. The array size of the model is kept the same for experiments of the same type so that the integration domain is expanded in proportion to the grid size. Along the north and south sides of the domain there is no flow across the boundary. On the east and west sides the tendencies boundary-condition treatment by Perkey and Kreitzberg (1976) is used. In general, this boundary condition uses a blending method within five grid points from the outermost point where the tendency is specified or provided from a forecast of a larger-domain model. Within the blending zone, a linear weighting factor is applied so that the innermost grid points use the tendencies from the hydrostatic model. In our application of this method, the outermost tendency is zero on

both the east and west sides. The vertically propagating waves are partially damped by allowing the second-order diffusion coefficient to increase linearly from a constant value of $4 \times 10^4\ m^2\ s^{-1}$ over the lowest 11 levels to 1.9 times that value at the top level.

(c) *Topography*

In order to compare our results with other studies, we use the mountain profile of Smith (1979b):

$$H(x, y) = \frac{h}{(1 + x^2/a_{ox}^2 + y^2/a_{oy}^2)^{3/2}} \tag{2.1}$$

where h is the maximum height of the mountain, and a_{ox} and a_{oy} are the mountain scales in the x and y directions respectively. This mountain profile is given in Fig. 1. Smith (1979b) and Smolarkiewicz and Rotunno (1989, 1990; hereafter SR89, SR90) use a_{ox} as the characteristic length L of the mountain. Pierrehumbert and Wyman (1985) and Blumen and Gross (1987) use the Gaussian distribution, and the half-mountain width is chosen as the characteristic length. The half width for the mountain profile described in (2.1) is about $0.7a_{ox}$, so there is some difference in determining L when computing Ro. From (2.1), the horizontal mountain-aspect ratio is (a_{ox}/a_{oy}).

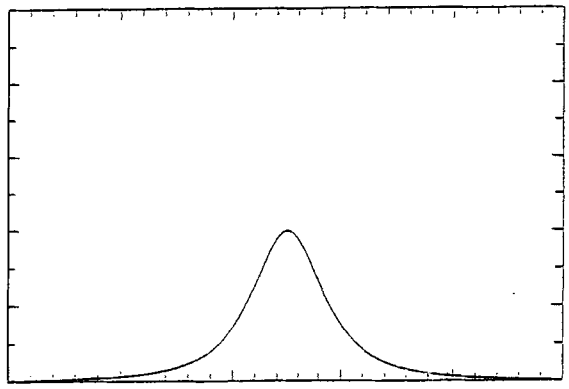

Figure 1. Vertical cross-section of the mountain profile as prescribed by Eq. (2.1), following Smith (1979b).

The basic state for all experiments consists of a prescribed uniform westerly flow in geostrophic balance that is embedded in a standard atmosphere. The initial conditions are first given in pressure coordinates with a tropopause at 100 hPa with a constant temperature above and a constant lapse rate below. The mountain is introduced into the uniform flow by interpolation from pressure to σ surfaces of the numerical model. This impulsive start will generate transient disturbances in some experiments. In certain cases the mountain height is raised gradually during the first part of the integration in order to represent more closely the steady-state problem.

The purpose of each experiment and the corresponding parameters are listed in Table 1.

3. Effects of the Coriolis force for flows over small-scale mountains

For flow over small-scale mountains, Ro is large, so that the Coriolis force has usually been neglected in previous studies. The behaviour of the flow over the mountain

TABLE 1. DESCRIPTION OF EXPERIMENTS AND PARAMETERS

Experiment	U (m s^{-1})	h (m)	f (s^{-1})	a_{ox} (km)	a_{oy} (km)	Rossby number	Froude number	Purpose
1a	10	2000	0	25	25	—	0.5	Coriolis effect
1b	10	2000	10^{-4}	25	25	4	0.5	Coriolis effect
2a	10	2000	0	50	50	—	0.5	Coriolis effect
2b	10	2000	10^{-4}	50	50	2	0.5	Coriolis effect
3	10	2500	0	300	300	—	0.4	Scale effect
4a	10	1000	0	25	25	—	1	Coriolis effect
4b	10	1000	10^{-4}	25	25	4	1	Coriolis effect
5a	5	2000	10^{-4}	100	100	0.5	0.25	Scale effect
5b	5	2000	10^{-4}	200	200	0.25	0.25	Scale effect
5c	5	2000	10^{-4}	300	300	0.167	0.25	Scale effect
5d	5	2000	10^{-4}	400	400	0.125	0.25	Scale effect
6a	10	2000	10^{-4}	100	100	1.0	0.5	Scale effect
6b	10	2000	10^{-4}	200	200	0.5	0.5	Scale effect
6c	10	2000	10^{-4}	300	300	0.334	0.5	Scale effect
6d	10	2000	10^{-4}	400	400	0.25	0.5	Scale effect
7	10	2000	10^{-4}	300	900	0.33	0.5	Shape effect
8	10	0–2000	10^{-4}	300	900	0.33	0.5	Shape effect
9	5	2000	10^{-4}	300	900	0.16	0.25	Shape effect
10	10	2000	10^{-4}	960	1920	0.104	0.5	Scale effect
11	5	2000	10^{-4}	960	1920	0.052	0.25	Scale effect
12	5	0–2000	10^{-4}	960	1920	0.052	0.25	Scale effect
13	10	2000	10^{-4}	180	—	0.56	0.5	3-D effect
14	5	1000	10^{-4}	68	—	0.74	0.5	3-D effect

See text for explanation of column headings.

is then determined solely by Fr which measures the ratio between the kinetic energy of the parcel upstream, and the energy required to lift the fluid over the mountain. For large Fr, the linear theory for 2D flow developed in the pioneering works of Lyra (1943) and Queney (1948) applies. In this regime most of the flows have enough energy to climb over the mountain, and gravity waves are generated on the lee side. The corresponding solutions for 3D flow are given by Smith (1980). When Fr is very small, Drazin (1961) shows that the flow over the mountain reduces to potential flow. Even though the Drazin solution is not complete, it does describe the flow in that limit. Generally, when Fr is small, the flow does not have enough energy to climb over the mountain and the flow is relatively horizontal. When the air flows around the mountain in a horizontal plane, no mountain waves are generated.

SR89 and SR90 use a high-resolution nonhydrostatic numerical model to study flows over small-scale mountains, with moderate values of Fr to fill in the gap between linear theory and potential flow. Figure 3 in their study (SR89) displays the flows as a function of Fr, with $f = 0$. They show that a pair of symmetric vortices are generated on the lee side when Fr is smaller than 0.5. Hunt and Snyder (1980) hypothesize that the lee vortices are generated within the viscous boundary layer and then sheared off. Results from SR89 indicate that, at least within a certain range of Fr, lee vortices can be generated without surface friction.

To study the effect of the Coriolis force on flow over small-scale mountains, we compare our model simulations with and without the Coriolis force in the same parameter range as SR89 and SR90. In experiment 1, we choose $a_{ox} = a_{oy} = 25$ km, $U = 10$ m s^{-1}, and $h = 2000$ m. The Brunt–Väisälä frequency, N, is equal to 10^{-2} s^{-1} for all experiments, which gives $Fr = 0.5$ for experiment 1. Note that the width of the mountain in this experiment is the same as the one in SR89. $Fr = 0.5$ is chosen for our presentation, which

is roughly the upper bound of Fr where lee vortices can be induced without a viscous boundary layer (SR89). The flow fields on our model's lowest and second-lowest levels at $t = 8$ h are shown in Fig. 2. The left panels are solutions for $f = 0$ and the right panels are for $f = 10^{-4}\text{s}^{-1}$ ($Ro = 4$). Even with this large Rossby number the flows with and without f are not the same. Without f, Fig. 2(a) shows a stagnation point on the upwind side and a reversal of flow upstream. In Fig. 2(a), with $Fr = 0.5$, upstream-propagating flow meets the constant incoming flow, and a region with irregular flow occurs at the place when these two flows meet. This irregularity does not occur in solutions shown in SR89 and SR90 when $Fr < 0.5$. In experiment 1a with $f = 0$, there are a pair of symmetric vortices on the lee side (Figs. 2(a) and (b)), in agreement with SR89.

With the Coriolis force included in experiment 1b, the flow is asymmetric and is always deflected more to the left on the upstream side (Figs. 2(c) and (d)). The upwind left deflection is treated analytically by Smith (1982) based upon an expansion for large

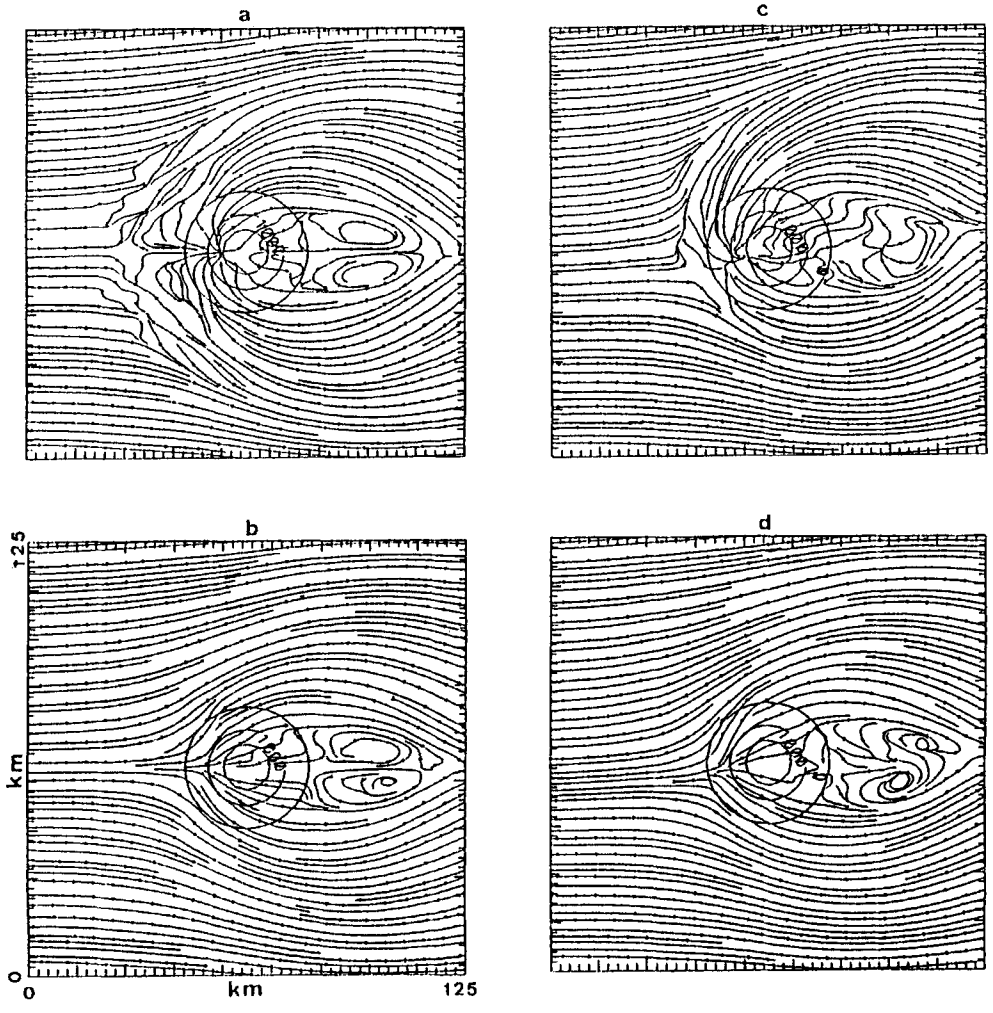

Figure 2. Horizontal streamlines at $t = 8$ h for flow over a small-scale mountain; (a) and (b) without the Coriolis force and (c) and (d) with the Coriolis force, $a_{ox} = a_{oy} = 25$ km, $U = 10\text{ m s}^{-1}$ and $h = 2000$ m. $Fr = 0.5$ and $Ro = 4.0$ for (c) and (d). (a) and (c) are at the model's lowest level where $\sigma = 0.9975$, (b) and (d) are at the model's second-lowest level where $\sigma = 0.9775$. See text for explanation of symbols.

Rossby number (Fig. 2(c)). Due to the deflection of the flow by the Coriolis effect, there is little upstream propagation of the reversed flow except for a diffluent region. The vortices on the lee side in Figs. 2(c) and 2(d) do not have the symmetric structure that occurs for the $f = 0$ case in Figs. 2(a) and 2(b). Furthermore, these vortices are not steady, in contrast with those shown in SR89 for $f = 0$. Instead, they drift gradually away from the mountain in our experiments, in agreement with the numerical simulation by Crook *et al.* (1990) for the Denver cyclone. In experiment 2, the mountain size measured by a_{ox} is doubled while keeping the other variables the same as in experiment 1. The flow patterns with and without the Coriolis force show more significant differences as expected (Fig. 3). The lee vortices are highly asymmetric and there is no reversal flow upstream when the Coriolis force is included. The upstream irregularity in Fig. 2 is not present in Fig. 3. Note that flows at higher levels of the model experience smaller influence from the Coriolis force. This may be due to the fact that the flows at higher

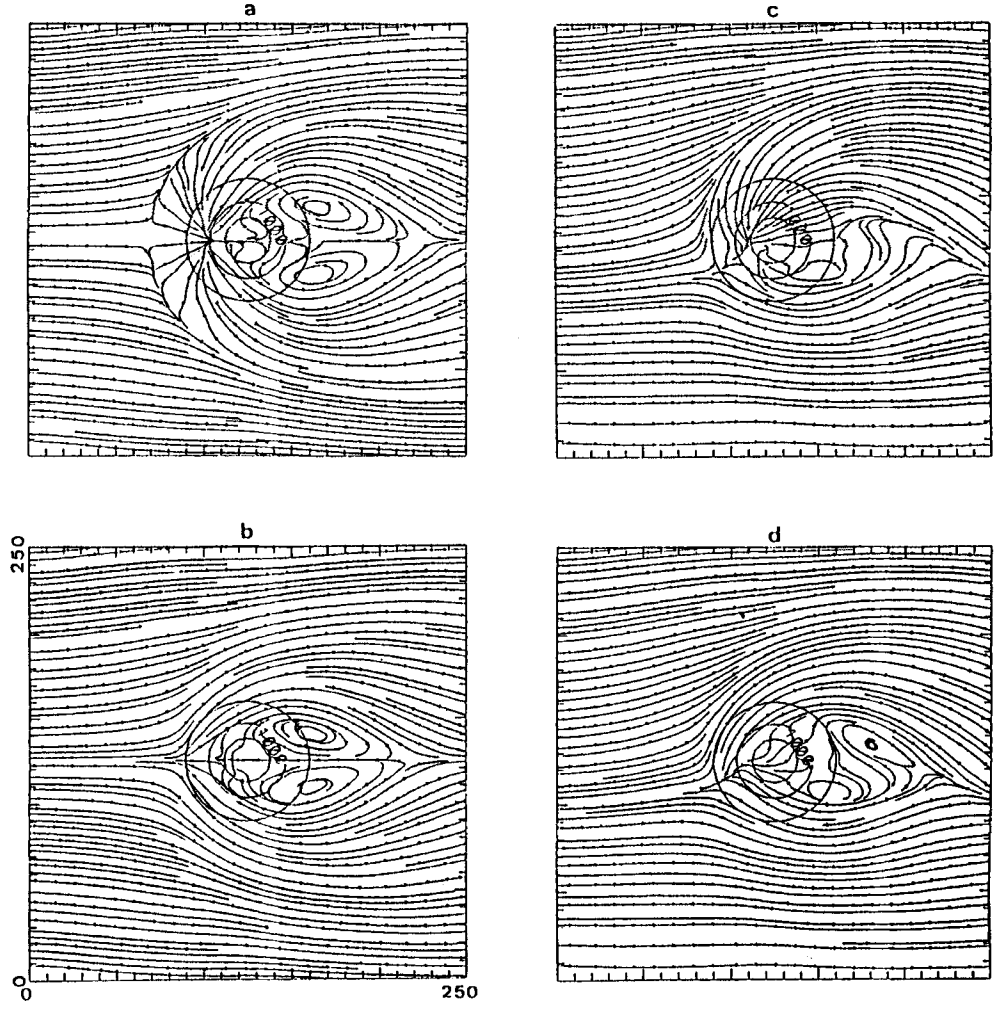

Figure 3. Same as in Fig. 2 except $a_{ox} = a_{oy} = 50$ km at the model's lowest level where $\sigma = 0.9975$. In this case $Ro = 2.0$ for flow in panels (b) and (d).

levels do not have to climb as much to go over the mountain and they feel less deflection by the Coriolis effect.

A disturbance would propagate infinitely far upstream in a 2D framework without f (Pierrehumbert and Wyman 1985). Pierrehumbert and Wyman (1985) further hypothesize that in a 3D model the upstream influence would have a length-scale determined by the Rossby radius of deformation when f is included. This is, however, not consistent with our results because it implies large upstream influence when f is small, which we do not observe.

The horizontal length-scale of the lee vortices is proportional to the mountain length-scale in the cross-flow direction (a_{oy}) for non-circular mountains, as indicated by Fig. 11 in SR90. These lee vortices exist as long as $f = 0$ and Fr is roughly within the range of 0.1 to 0.5 irrespective of the scale of the mountain. Experiment 3 with $a_{ox} = a_{oy} = 300$ km, $U = 10\ \mathrm{m\ s^{-1}}$, $f = 0$ and $h = 2500$ m ($Fr = 0.4$) is shown in Fig. 4. There is little difference between this pattern and those associated with much smaller mountains shown in SR90 and Figs. 2 and 3.

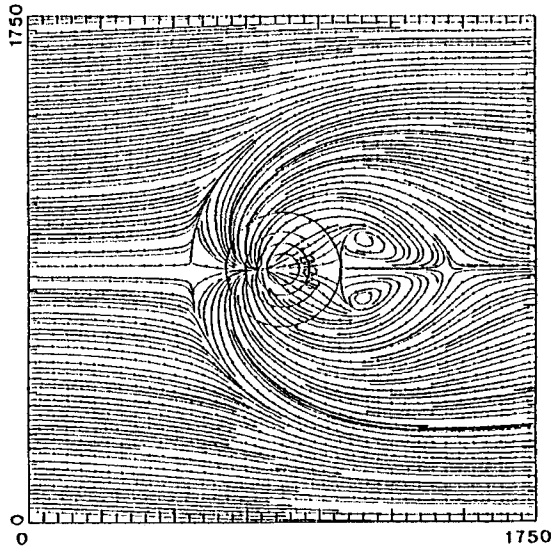

Figure 4. Streamlines for flow over a medium-scale circular mountain with $a_{ox} = a_{oy} = 300$ km, $h = 2500$ m, $U = 10\ \mathrm{m\ s^{-1}}$ and $f = 0$. The grid size is 50 km. See text for explanation of symbols.

The effect of the Coriolis force on flow over a small-scale mountain depends on whether most of the airflows are over or around the mountain. To illustrate this, the mountain height is decreased to 1000 m in experiment 4 while keeping the other parameters the same as in experiment 1. This doubles Fr from 0.5 to 1.0 while keeping Ro the same. In this case most of the flow has the momentum to go over the mountain, and the difference between flows with and without the Coriolis force is small (Fig. 5). This indicates that, in examining the importance of the Coriolis force, it is necessary to consider both Fr and Ro.

The downslope wind and gravity waves are less influenced by the Coriolis force. In general, the Coriolis force has less effect on lee-side phenomena that are induced by flow over the mountain.

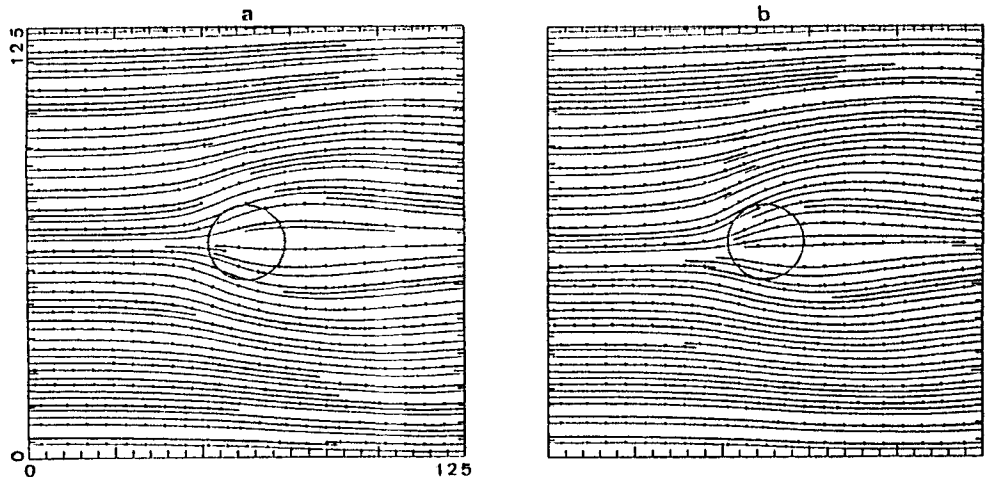

Figure 5. Same as in Fig. 2 except the mountain height $h = 1000$ m; (a) $f = 0$ and (b) $f = 10^{-4}$ s^{-1}. Solutions are at the model's lowest level where $\sigma = 0.9975$. In this case, $Fr = 1.0$ and $Ro = 4.0$ for flow in panel (b).

4. Flows over mesoscale to synoptic-scale mountains

There are only a few studies of flow over 3D mesoscale mountains in the literature. Smith (1982) extends his own linear solution for an isolated mountain (Smith 1980) to include the Coriolis effect with an expansion in the reciprocal of Ro, which is required to be large. In his solution a pressure increase is induced upstream and a pressure decrease is induced downstream of the mountain. When a parcel approaches the high pressure on the windward side, it decelerates and the flow is no longer in geostrophic balance. The slower-moving parcel feels a decreased Coriolis force and the pressure-gradient force sends it to the left. Meanwhile, a cyclonic circulation forms on the lee side.

In this section we examine flows over or around mountains ranging from mesoscale to synoptic scale, to show how the flow pattern changes as the horizontal mountain scale increases. All experiments discussed from this point contain the Coriolis force. In experiments 5a–5d, the mountain shape is circular and the values of a_{ox} and a_{oy} increase from 100 km to 400 km with an interval of 100 km. The uniform mean flow $U = 5$ m s^{-1}, $f = 10^{-4}$ s^{-1} and the mountain height $h = 2000$ m are kept the same. Therefore, $Fr = 0.25$ for all of these cases, while Ro takes the values 0.5, 0.25, 0.1666, and 0.125, respectively. Figure 6 shows the horizontal streamlines at the model's lowest level for $t = 48$ h. In Fig. 6(a), with $a_{ox} = a_{oy} = 100$ km, the flow field is similar to the small-scale mountain discussed in section 3. However, on the upstream side the flow is deflected more to the left, and on the lee side the vortices are more asymmetric. The stronger flow around the north side of the mountain contributes to the stronger vortex on the north side. As the mountain scale is increased to 200 km ($Ro = 0.25$), a lee trough is developed by flow around the mountain (Fig. 6(b)), in agreement with the theory of Smith (1982). With $Ro = 0.25$ in this experiment, the Coriolis effect dominates and lee vortices do not develop even though Fr (=0.25) is within the critical range of lee-vortex development (SR89). Instead, only a lee-side confluent zone exists. As the mountain size is further increased to 300 km and $Ro = 0.1666$ (experiment 5c), the lee-side trough is well organ-

ized and attached to the southern side of the mountain (Fig. 6(c)). The flow converges anticyclonically over the mountain to a central point located south-east of the mountain crest. Experiment 5d (Fig. 6(d)) with a_{ox} = 400 km and Ro = 0.125 is similar to experiment 5c (Fig. 6(c)). The anticyclonic circulation over the mountain is now more symmetric with respect to the mountain, and the flow pattern is similar to the one predicted by semi-geostrophic theory (Merkine and Kalnay-Rivas 1976; Blumen and Gross 1987).

In experiments 6a–6d, the basic wind speed is increased to 10 m s^{-1} while all the other parameters are the same as in experiments 5a–5d, therefore, Fr = 0.5 and Ro = 1.0, 0.5, 0.333, 0.25, respectively (Fig. 7). In this parameter range, the lee vortices shrink into a small confluent zone in experiments 6a–6c (Figs. 7(a)–7(c)) and they are embedded within the lee trough. In experiment 6d, there is no confluent zone (Fig. 7(d)). Two troughs are generated in experiment 6d as compared with one trough in 5d (Fig. 6(d)). The first trough, generated by flow over the mountain, is transient and moves away from the mountain. The second trough, generated by flow around the mountain,

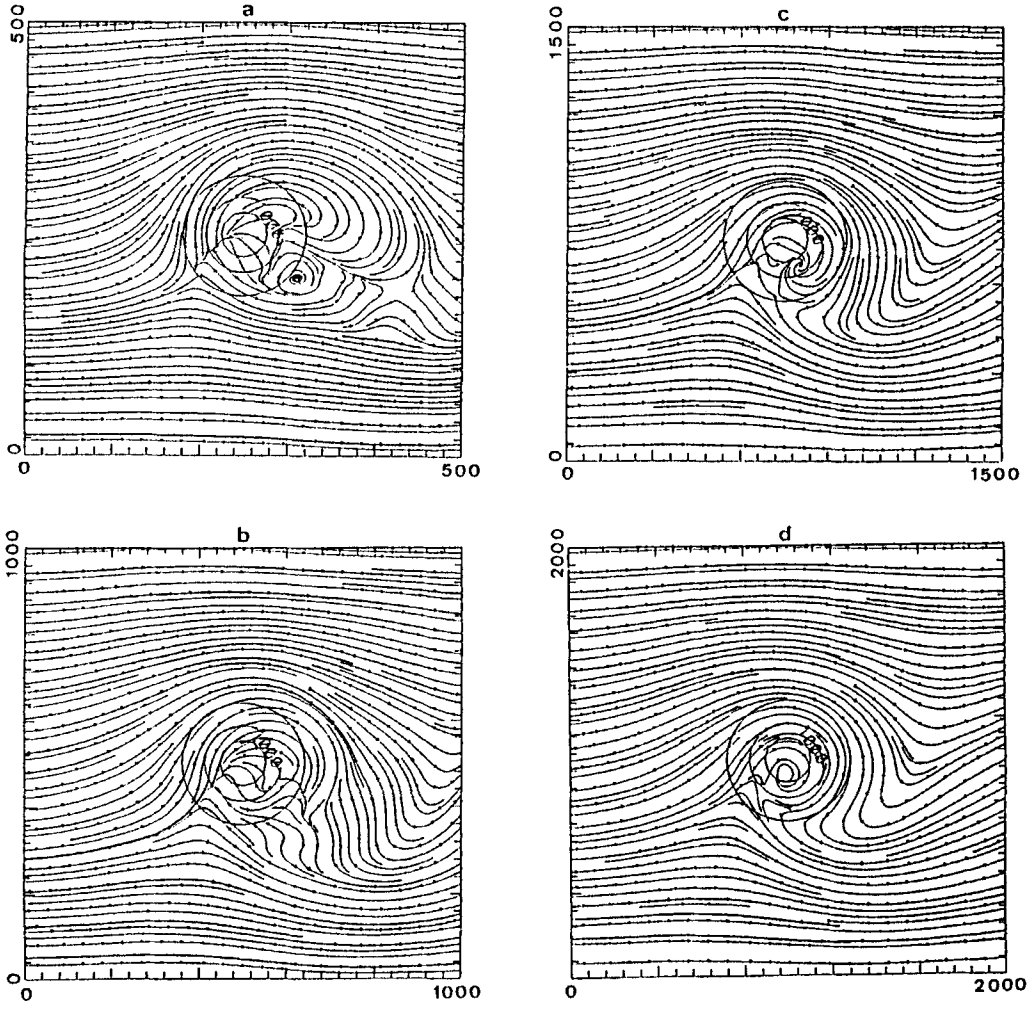

Figure 6. Flow patterns at t = 48 h for circular mountains with difference scales; (a) $a_{ox} = a_{oy}$ = 100 km, (b) $a_{ox} = a_{oy}$ = 200 km, (c) $a_{ox} = a_{oy}$ = 300 km, and (d) $a_{ox} = a_{oy}$ = 400 km. In all cases, h = 2000 m and U = 5 m s^{-1}. See text for explanation of symbols.

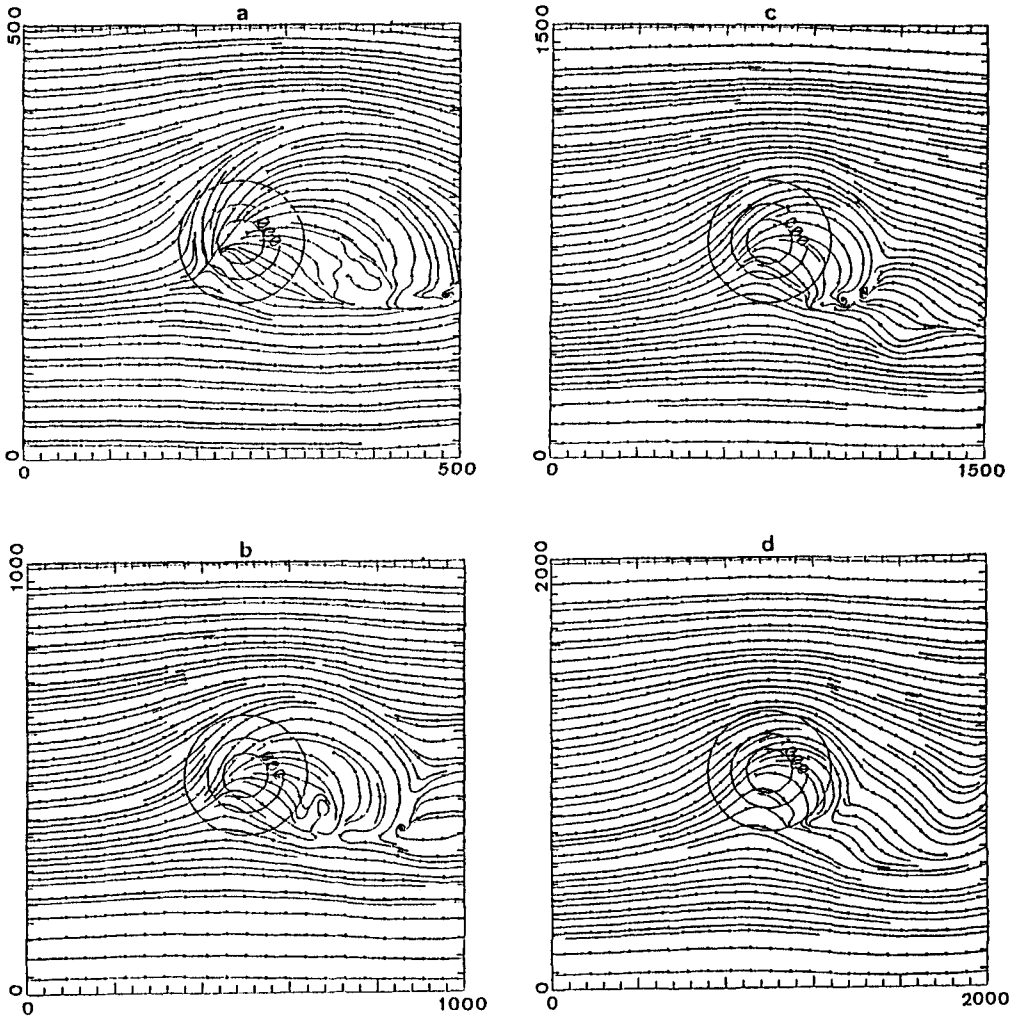

Figure 7. Same as in Fig. 6 except $U = 10\ \mathrm{m\ s^{-1}}$.

attaches to the mountain. Note that the upstream flows are similar for all the cases in Figs. 6 and 7. The vertical potential-temperature profile corresponding to Fig. 7 shows more gravity-wave activity since the flow speed is larger (figures not shown).

Experiment 7 is designed for flow over a mesoscale elliptic mountain with $a_{ox} = 300$ km, $a_{oy} = 900$ km, $U = 10\ \mathrm{m\ s^{-1}}$. Figure 8 shows the time series for flow fields at the model's lowest level. In Fig. 8(a), the first trough is generated on the lee side at 24 h. This trough moves downstream and a second trough develops at $t = 48$ h at the same location as the first one (Fig. 8(b)). As the second trough moves away, a third trough forms at $t = 72$ h (Fig. 8(c)). As time goes on, a series of troughs are generated on the lee side and propagate downstream. The wave length of the lee-trough train is about equal to the cross-stream mountain scale. The first trough later separates into two troughs. The one located to the north has a larger scale and it propagates downstream faster than the southern one. As in experiment 6d (Fig. 7(d)), the first trough, which

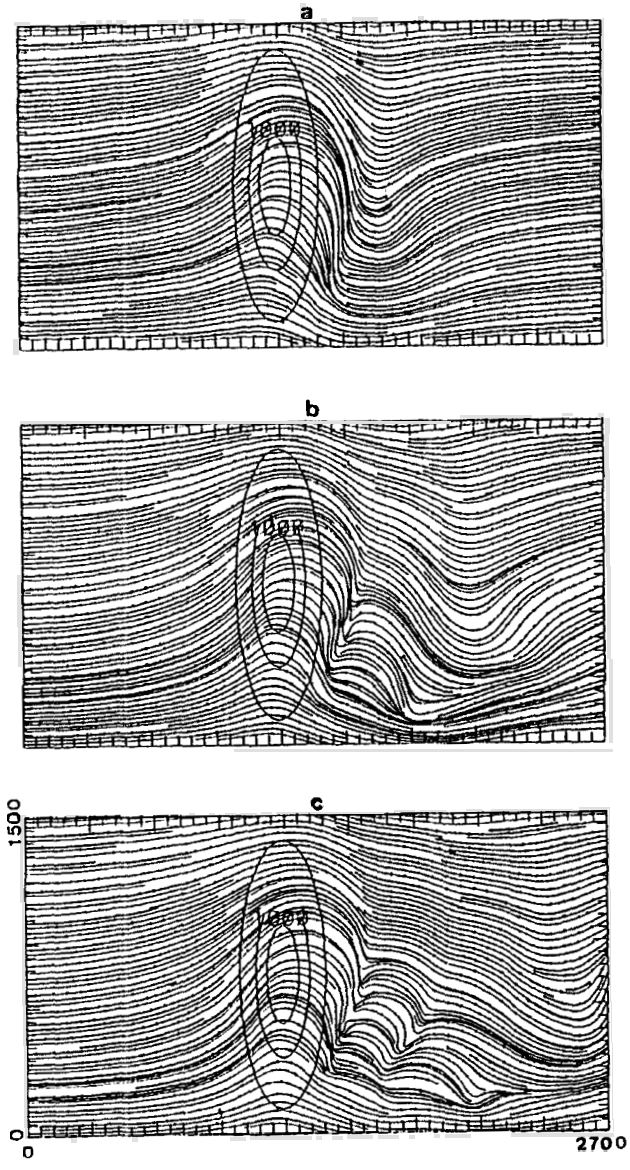

Figure 8. Streamlines at the model's lowest level for flow over a medium sized long mountain with $U = 10\ \mathrm{m\ s^{-1}}$, $h = 2000$ m, $a_{ox} = 300$ km and $a_{oy} = 900$ km; (a) $t = 24$ h, (b) $t = 48$ h and (c) $t = 72$ h. See text for explanation of symbols.

moves faster and is located more to the north, is the warm-core start-up vortex that results from displacing the air initially over the mountain into the lee, when a uniform flow suddenly impinges on the mountain (Huppert and Bryan 1976; Smith 1979a). In a supplementary experiment (experiment 8), the mountain height increased gradually from $t = 0$ to its maximum during the initial 24 hours of integration. The flow field at $t = 84$ h is shown in Fig. 9(a) and it is to be compared with the flow at 72 h in Fig. 8(c). In this case, the first fast-moving, deeper trough does not appear, while the trailing troughs are similar to the one in experiment 5.

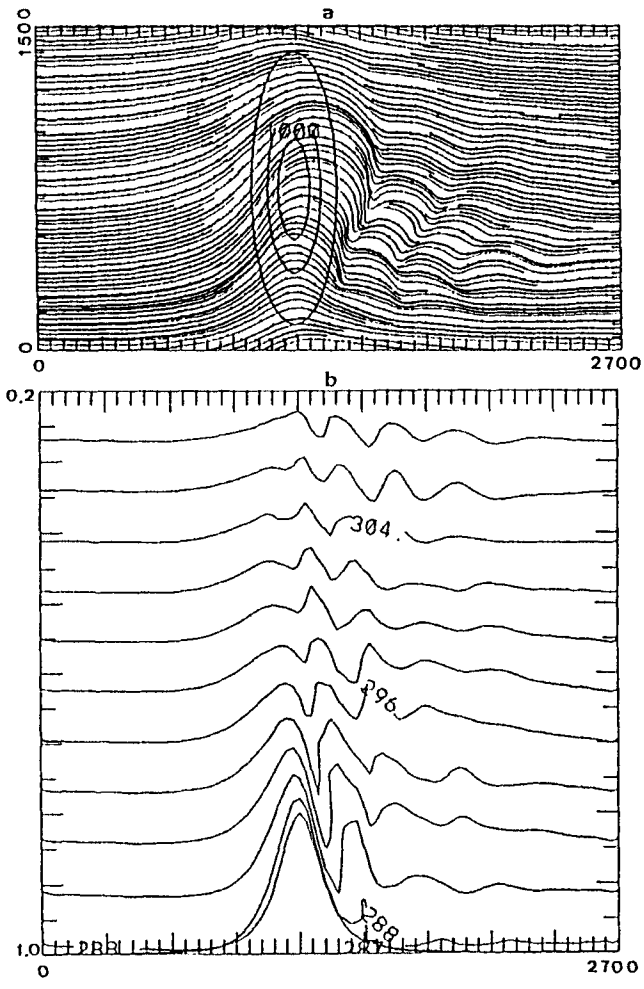

Figure 9. (a) Same as in Fig. 8 for t = 84 h except the mountain height is increased to its maximum height gradually in the first 24 h of integration. (b) Vertical cross-section of the potential temperature on σ levels along the centre of the mountain.

The mechanics associated with the wave train of troughs is different from the trough generated by an impulsive start. Examination of the vertical cross-section of potential temperature across the centre of the mountain indicates that these low-level troughs are associated with the lee-side gravity waves (Fig. 9(b)). When the upstream mean flow is reduced from 10 m s^{-1} in experiment 7 to 5 m s^{-1} in experiment 9, the lee-side gravity waves and low-level wave train propagate more toward the south (Fig. 10). The vertical velocities at the model's second-lowest level, corresponding to Fig. 8(c) and Fig. 10, are given in Fig. 11, which shows more clearly the orientation and propagation of the travelling troughs relative to the mountain. When a flow crosses a 2D mountain, the lee-side gravity wave induced by flow over the mountain always propagates in the same direction as the upstream impinging flow. Over the 3D mountain, the propagation direction of a lee-side gravity wave is not necessarily the same as the upstream flow. Instead, depending on the mountain scale and mean flow speed, it propagates more

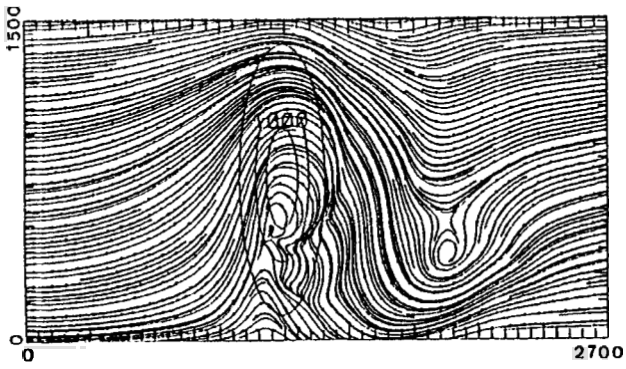

Figure 10. Same as in Fig. 8(c) for $t = 72$ h except $U = 5\ \mathrm{m\ s^{-1}}$.

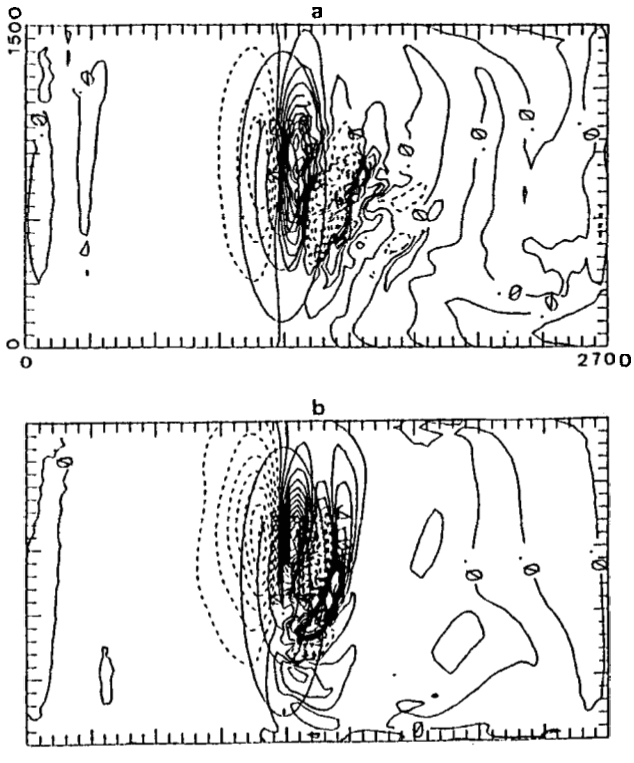

Figure 11. Vertical velocity for (a) Fig. 8(c) and (b) Fig. 10.

toward the south. This indicates that more flow is blocked or deflected to the north before it goes over the mountain.

In summary, the model results suggest that as the horizontal scale of the mountain increases, lee vortices shrink and eventually disappear and, in the meantime, the lee trough starts to appear. The length-scale of the lee trough is proportional to the mountain scale in the along-flow direction (a_{ox}). Note that this scale dependence is different from that of the lee vortices in which the scale depends on the mountain scale in the cross-

flow direction (a_{oy}). The difference arises because the lee vortices and the lee troughs are caused by different mechanisms. The length-scale for the train of troughs is determined, however, by the mountain scale in the cross-flow direction (a_{ox}), as can be expected by the trough-generation mechanism. On the upstream side, as the mountain scale increases, flow splitting decreases and the flow is deflected to the left. It is not surprising that flows in the transitional range seem to have the dual character of flows over small- and larger-scale mountains.

5. Flows over large-scale mountains

In this section we will examine flow over large-scale ($L \sim 1000$ km) mountains with different initial conditions. A brief review of previous analytic theories is given here to provide background. When Ro is small, the mountain circulation can be obtained from quasi-geostrophic theory. Smith (1979a) shows that in a vertically unbounded domain, conservation of quasi-geostrophic potential vorticity requires anticyclonic circulation over the mountain with decreasing strength with height. Merkine (1975) treats 2D flow over an infinite ridge with an upper lid using a semi-geostrophic model which includes the ageostrophic acceleration in the along-mountain direction. The solution shows that the flow is permanently deflected to the right on the lee side of the mountain ridge. The deflection is accompanied by a low-pressure region. This deflection is due to the upper rigid lid and the conservation of potential vorticity. Pierrehumbert (1985) solved the semi-geostrophic equations for flow over an infinite ridge with no upper boundary, and found no permanent turning on the lee side.

The semi-geostrophic theory for flow over a 3D mountain is developed by Merkine and Kalnay-Rivas (1976) and by Blumen and Gross (1987). In their solutions an anticyclonic, bounded vortex occurs over an isolated circular mountain. When the strength of the vortex is sufficiently large, a closed vortex exists for a total field. In comparison with quasi-geostrophic flow, a rotational gradient-wind correction that is independent of the basic current is introduced. This enhances the maximum velocity over the ridge. The transformation of the semi-geostrophic solution from the geostrophic coordinate space to the physical space displaces the circulation feature on level surfaces radially outward from the vertical axis, and the displacement is proportional to the mountain height. Blumen and Gross (1987) show by a scale analysis that the semi-geostrophic approximation is good for $Ro < 0.3$ and $h/D < 0.5$, where h is the mountain height and D is the deformation depth ($D = fL/N$).

Experiment 10 is designed for flow over a large-scale elliptic mountain with $a_{ox} = 960$ km, $a_{oy} = 1920$ km, $U = 10\ \mathrm{m\ s^{-1}}$, $h = 2000$ m. Ro in this case is 0.1 and $h/D = 0.23$. In Figure 12 the lee-side trough is initiated as a warm-core start-up vortex from the impulsive initial flow and then it drifts away from the mountain. By 144 h, the flow pattern in the mountain area is nearly symmetric and it resembles the steady-state semi-geostrophic solution. The vertical-velocity pattern throughout this experiment is the same as the one shown in Fig. 12(d) for 144 h, indicating there is no flow around the mountain.

To explore further the lee-side low and trough, the mean flow speed is reduced from $10\ \mathrm{m\ s^{-1}}$ to $5\ \mathrm{m\ s^{-1}}$ in experiment 11, with the other parameters the same as in experiment 10. The streamlines and the vertical velocity at the model's lowest level are shown in Fig. 13. At 24 h (Figs. 13(a) and 13(d)), most of the flow goes over the mountain (as can be seen from the vertical-velocity pattern) and a trough starts to develop on the lee side. By 72 h (Figs. 13(b) and 13(e)), the vertical-velocity pattern has a quadruple form, indicating that the flow goes over as well as around the mountain. There is an anticyclonic

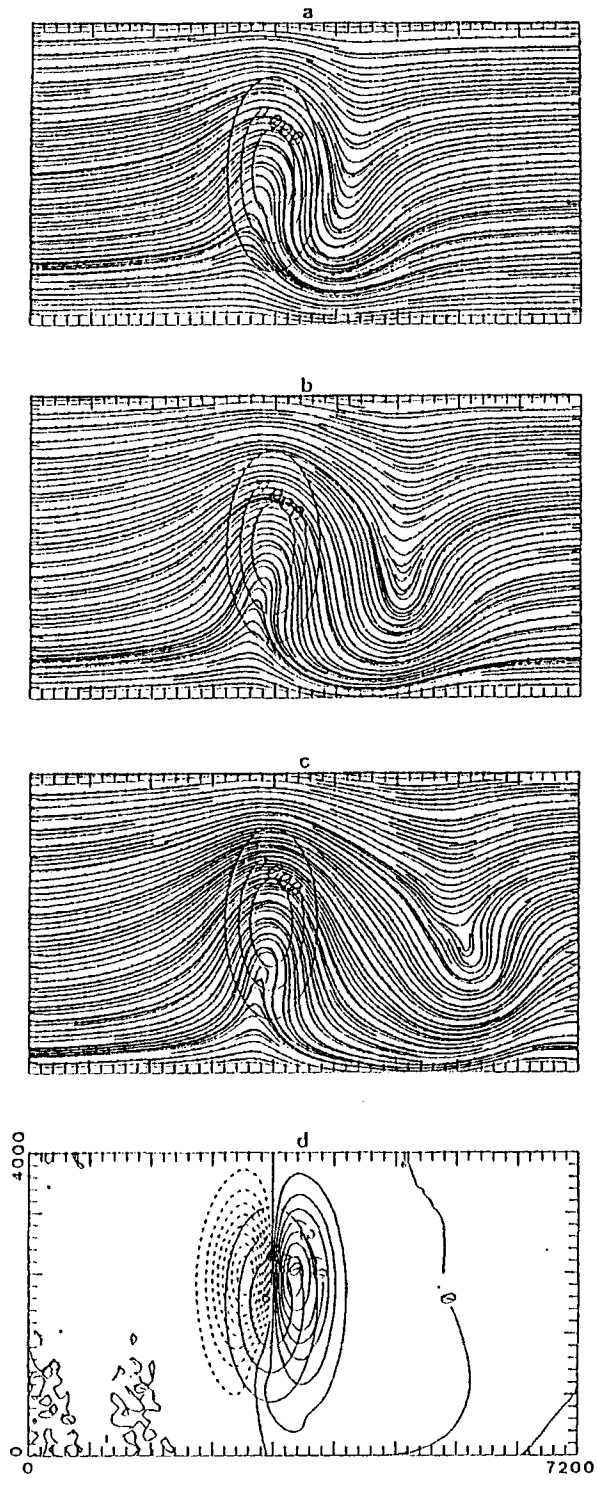

Figure 12. Flow over a large elliptic mountain with $U = 10\ \mathrm{m\ s^{-1}}$, $h = 2000$ m, $a_{ox} = 960$ km and $a_{oy} = 1920$ km: (a)–(c) are the streamline patterns for $t = 48$ h, 96 h and 144 h, respectively; (d) is the vertical velocity corresponding to $t = 144$ h with dashed lines indicating upward motion. See text for explanation of symbols.

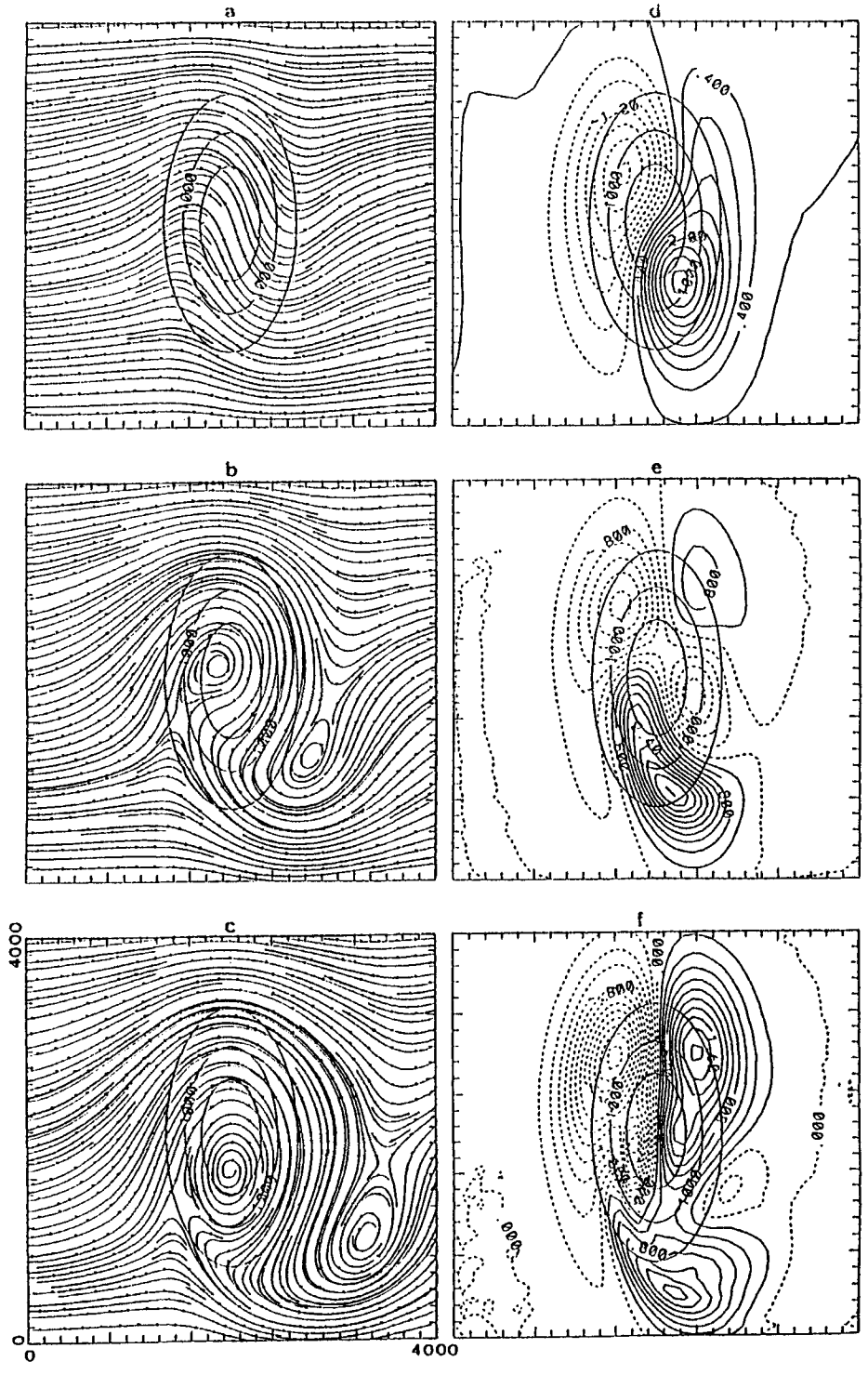

Figure 13. Same as in Fig. 12 except $U = 5\ \mathrm{m\ s^{-1}}$. The left panels (a)–(c) are the streamlines and the right panels (d)–(f) are the vertical velocity with dashed lines indicating upward motion and solid lines indicating downward motion. Top panels: $t = 24$ h, middle panels: $t = 72$ h and lower panels: $t = 144$ h.

vortex located slightly upwind of the mountain peak and a cut-off low within the lee-side trough. By 144 h (Figs. 13(c) and 13(f)), the streamline pattern shows a nearly symmetric anticyclonic vortex over the mountain. However, the southern and eastern parts of the flow pattern are still asymmetric. The lee-side low centre moves slightly downstream from the mountain, but the tip of the trough remains attached to the southern tip of the mountain.

The general behaviour that is seen in experiments 10 and 11 can be explained in terms of vorticity advection. In each case the warm-core start-up vortex is advected to the east by the mean flow, so that it separates from the topographically forced anticyclone over the mountain. In experiment 11 where the mean flow is weak, the cyclone (or trough) is advected first by the topographically forced anticyclonic flow to the south where the mean flow after passing the mountain is very weak (Fig. 13(b)). Thus, the cyclone remains attached to the south-east side of the mountain for a long time (Fig. 13(c)). When the mean wind is stronger (experiment 10), this southward advection by the anticyclonic flow is small compared with the westerly mean flow, so that the trough is advected away from the mountain (Fig. 12). The relative importance of these effects is measured by Fr because the north–south advection by the topographic anticyclone is proportional to the mountain height.

One of the hypotheses of lee cyclogenesis postulates that when the flow impinges on the mountain impulsively, the initial potential-temperature field over the mountain will be transported downstream and replaced by upstream air (Smith 1979a). The isentropic surfaces that initially intersect the terrain surface will introduce a warm-core cyclone on the lee side that moves downstream from the mountain. To substantiate this, in experiment 12, we repeat experiment 9 except that we increase the mountain height gradually from zero to its maximum of 2000 m in 24 hours. In this case the flow always follows the contour of the mountain and no quasi-geostrophic transients are excited. The flow at 72 h (Fig. 14(a)) shows a symmetric pattern with respect to the centre of the mountain and no lee trough is generated. A comparison of the vertical-velocity patterns in Figs. 13(e) and 14(b) indicates that, when the mountain is 'grown' gradually, all the flow goes over the mountain and there is no blocking effect. This is consistent with the analytic solution for a 2D mountain given by Bannon (1991).

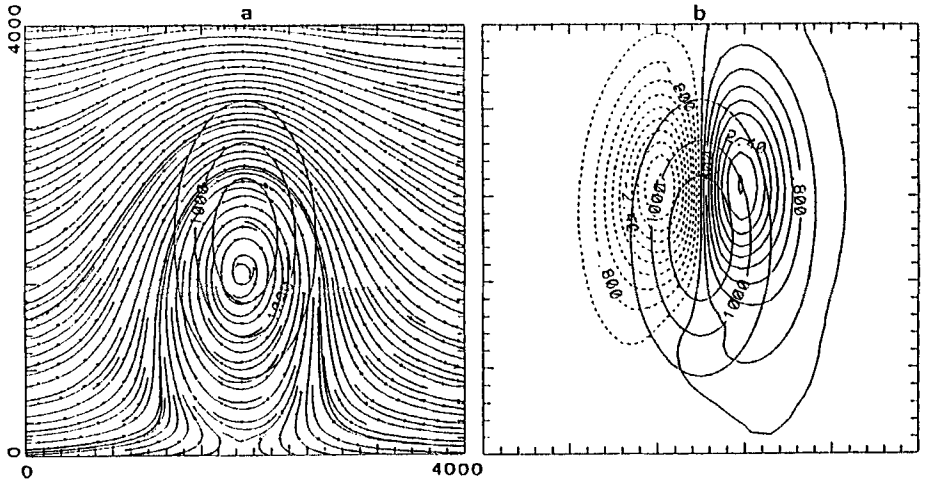

Figure 14. The same as in Fig. 13 for $t = 72$ h except the mountain height is increased gradually from zero to its maximum in 24 hour. The left panel (a) contains the streamlines and the right panel (b) the vertical velocity.

In 2D models all flows are forced to go over the mountain. If the initial wind field impinges on the mountain impulsively, the warm-core trough on the lee side will always propagate away from the mountain. Only if there is some flow around a 3D mountain that contributes to the formation of a lee trough will the trough remain attached to the mountain. This could provide a favourable environment for lee cyclogenesis, especially if the basic current is baroclinic.

6. Comparison of 2D and 3D mountain flows

The major difference between flows over 2D and 3D mountains is that in a 2D model all the flow is either forced to go over the mountain or it is totally blocked because no flow can go around the mountain. In a 3D model the flow can go around as well as over the mountain. Our objective here is to explore the range of horizontal mountain-aspect ratio (AR) in which the 3D solution approaches the 2D solution. For this purpose a 3D mountain profile with the same cross-section as the 2D mountain is used.

Experiment 13 has a mountain with a cosine-squared profile in both the x and y directions. This profile is chosen because it is used by Williams *et al.* (1992) in the 2D model in which strong downslope winds are generated on the lee side. The half width of the mountain is $L = 180$ km, $h = 2000$ m, and $U = 10\ \mathrm{m\ s^{-1}}$. Both the 2D and 3D models have the same horizontal grid size of 40 km and 36 levels in the vertical. For comparison, the cross-mountain surface wind speeds for the 2D mountain and for the 3D mountain (along its central latitude) are plotted in Fig. 15 for different AR. All three curves in Fig. 15 have a similar pattern of strong downslope winds and a small region of reversed flow further east. The maximum wind speed of $37\ \mathrm{m\ s^{-1}}$ is reached both over the infinite ridge (2D) and over the long mountain range with AR = 18/125. On the other hand, a maximum of only $30\ \mathrm{m\ s^{-1}}$ is reached for the shorter mountain (AR = 18/60). The reversed flows at the base on the lee side of the two 3D mountains are both stronger than for the infinite ridge. This is because the 3D flow around the mountain can contribute to the reversed flow on the lee side.

In experiment 14 the mountain size is reduced to a half-width of $L = 68$ km with $U = 5\ \mathrm{m\ s^{-1}}$ and $h = 1000$ m. The horizontal grid size is 5 km in this case. The three cross-mountain wind-speed curves shown in Fig. 16 are still similar to each other, but the differences between them are larger than those in experiment 13. The maximum wind speed across the mountain for the 2D mountain reaches $19.5\ \mathrm{m\ s^{-1}}$ (solid line). The flow over the 3D shorter mountain with AR = 18/60 (dotted line) has a maximum wind speed of $11.5\ \mathrm{m\ s^{-1}}$, which is 42% less than that of the infinite ridge. Over a longer mountain with AR = 18/125 (dashed line), the maximum wind speed reaches $16.8\ \mathrm{m\ s^{-1}}$, 14% less than that of the infinite ridge.

The Froude numbers for flows in experiments 13 and 14 are the same ($Fr = 0.5$). However, the mountain half-width in the former one is roughly three times that of the latter. As discussed in the previous section, the smaller the horizontal mountain scale, the easier it is for the flow to go around the mountain. Therefore, using a 2D model for the study of flow over a finite small-scale mountain range may overestimate lee-side phenomena such as the downslope wind.

7. Summary

In this paper we have explored some problems in flows over mountains that previously have not been studied in detail. The first problem concerns the Coriolis effect for flows over small-scale mountains. Other studies on this scale neglect the Coriolis

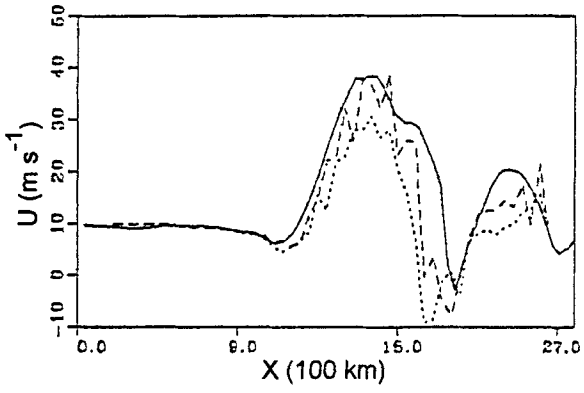

Figure 15. Cross-mountain surface wind after 60 h at the model's lowest level for $U = 10\,\mathrm{m\,s^{-1}}$, $h = 2000\,\mathrm{m}$ and $L = 180\,\mathrm{km}$. The solid line is from the two-dimensional model, the dashed line is from the three-dimensional model with aspect ratio (AR) = 18/125 (a very elongated mountain) and the dotted line is from a shorter mountain range with AR = 18/60. The mountain is located at the centre of the x axis. See text for explanation of symbols.

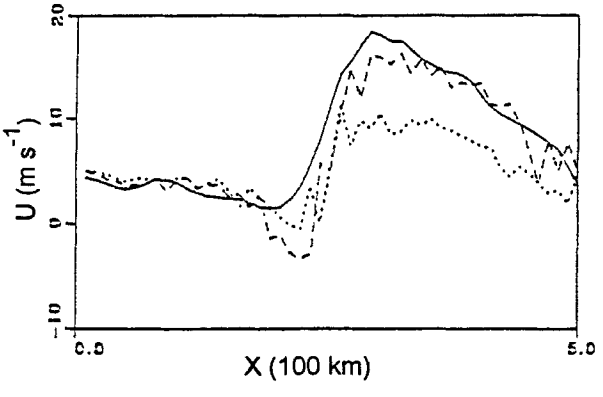

Figure 16. Same as in Fig. 15 but after 24 h and for a smaller mountain with $L = 68\,\mathrm{km}$ and $U = 5\,\mathrm{m\,s^{-1}}$, $h = 1000\,\mathrm{m}$.

force since the Rossby number is large as determined by the small length-scale of the mountain. When $f = 0$, a pair of symmetric lee-side vortices form when Fr is less than 0.5 (SR89). With the Coriolis force, the lee-side vortices are deformed, the upstream propagation is significantly reduced, and the upstream flow is deflected to the left side (Smith 1982). Also the vortices drift away from the mountain when f is present. When Fr is large and most of the flow goes over the mountain instead of around the mountain, the effect of the Coriolis force is small. Therefore, it is necessary to consider both Fr and Ro in determining the importance of Coriolis effects.

The flow pattern changes gradually as the horizontal scale of the mountain increases. Lee-side vortices are generated by flows around the mountain when both the mountain scale and Fr are small. The northern lee vortex is enhanced by the Coriolis force while the southern vortex shrinks. As the mountain width increases, the scale of the lee-side vortices decreases, and a lee-side trough, which contains the vortices, develops. As the mountain scale is further increased, an anticyclonic vortex develops over the mountain top when the mean wind speed is small. The lee-side trough originates as the warm-core

cyclone from the impulsive start-up initial condition. When the mean flow speed is small, the low centre is advected southward by the anticyclonic flow around the mountain to a position where the westerly flow is even weaker. In this case, the low centre or trough remains attached to the southern side of the mountain for a long time. When the mean flow is larger, the lee trough is advected downstream away from the mountain.

An elliptical shaped mesoscale mountain generates a train of lee troughs that are associated with the mountain-induced gravity waves. For a 3D mountain, the mountain-induced gravity waves do not necessarily propagate in the direction of the upstream flow as in a 2D model. Instead, depending on the speed of the upstream mean flow, the gravity waves propagate more to the south.

Numerical simulations with 2D and 3D models with the same mountain cross-section were performed. The results suggest that for mountains with the same horizontal aspect ratio, the infinite-ridge approximation is better when the horizontal scale is larger. As an example, mesoscale mountains with horizontal aspect ratio smaller than 1/4 can be approximated by an infinite ridge with less than 20% difference in the cross-mountain flow. For smaller-scale mountains ($L < 100$ km), more flow goes around the mountain, and accuracy of the infinite-ridge approximation decreases substantially. Therefore, the use of an infinite ridge overestimates the downslope wind when the mountain scale is small.

An impulsive flow with a moderate wind speed over a large-scale mountain generates a warm-core lee-side trough that will be advected downstream away from the mountain. On the other hand, a weaker mean flow can be partially blocked, and the anticyclonic flow around the mountain can advect the warm-core cyclone southward so that it remains attached to the southern tip of the mountain for a long time. This more stationary lee trough may be a prerequisite for lee cyclogenesis.

Acknowledgement

The authors wish to express their appreciation to three anonymous reviewers for their valuable comments and suggestions that led to an improvement of the manuscript. This research was in part supported by the National Science Foundation, Division of Atmospheric Science, under Grant ATM9106495. Some of the numerical calculations were carried out at the W. R. Church Computer Center of the Naval Postgraduate School.

References

Bannon, P. R. 1991 Rotating stratified flow over a mountain ridge as an initial value problem. *J. Atmos. Sci.*, **48**, 681–687

Blumen, W. and Gross, B. D. 1987 Semigeostrophic flow over orography in a stratified rotating atmosphere. Part I: Steady three-dimensional solutions over finite ridges. *J. Atmos. Sci.*, **44**, 3007–3019

Crook, N. A., Clark, T. L. and Moncrieff, M. W. 1990 The Denver cyclone. Part I: Generation in low Froude number flow. *J. Atmos. Sci.*, **47**, 2725–2742

Drazin, P. G. 1961 On the steady flow of a fluid of variable density past an obstacle. *Tellus*, **13**, 239–251

Durran, D. R. 1990 Mountain waves and downslope winds. Pp. 59–81 in *Atmospheric processes over complex terrain*. Ed. W. Blumen. American Meteorological Society, Boston

Hunt, J. C. R. and Snyder, W. H. 1980 Experiments on stably and neutrally stratified flow over a model three-dimensional hill. *J. Fluid Mech.*, **96**, 671–704

Huppert, H. E. and Bryan, K. 1976 Topographically generated eddies. *Deep-Sea Res.*, **23**, 655–679

Lyra, G.	1943	Theorie der stationaren Leewellenstromumg in freier Atmosphere. *Z. Angew. Math. Mech.*, **23,** 1–28
Madala, R. V., Chang, S. W., Mohanty, U. C., Madan, S. C., Paliwal, R. K., Sarin, V. B., Holt, T. and Raman, S.	1987	'Description of the Naval Research Laboratory limited area dynamical weather prediction model'. NRL Memorandum Report 5992, Naval Research Laboratory, Washington, DC
Merkine, L.-O.	1975	Steady finite-amplitude baroclinic flow over long topography in a rotating stratified atmosphere. *J. Atmos. Sci.*, **32,** 1881–1893
Merkine, L.-O. and Kalnay-Rivas, E.	1976	Rotating stratified flow over finite isolated topography. *J. Atmos. Sci.*, **33,** 908–922
Perkey, D. J. and Kreitzberg, C. W.	1976	A time-dependent lateral boundary scheme for limited-area primitive equation models. *Mon. Weather Rev.*, **104,** 744–755
Pierrehumbert, R. T.	1985	Stratified semigeostrophic flow over two-dimensional topography in an unbounded atmosphere. *J. Atmos. Sci.*, **42,** 523–526
Pierrehumbert, R. T. and Wyman, B.	1985	Upstream effects of mesoscale mountains. *J. Atmos. Sci.*, **42,** 977–1003
Queney, P.	1948	The problem of air flow over mountains: A summary of theoretical studies. *Bull. Am. Meteorol. Soc.*, **29,** 16–26
Smith, R. B.	1979a	Some aspects of the quasi-geostrophic flow over mountains. *J. Atmos. Sci.*, **36,** 2385–2393
	1979b	The influence of mountains on the atmosphere. Pp. 87–230 in *Advances in geophysics*, Vol. 21. Academic Press
	1980	Linear theory of stratified hydrostatic flow past an isolated mountain. *Tellus*, **32,** 348–364
	1982	Synoptic observations and theory of orographically disturbed wind and pressure. *J. Atmos. Sci.*, **39,** 60–70
	1989	Hydrostatic flow over mountains. Pp. 1–41 in *Advances in geophysics*, Vol. 31. Academic Press
Smolarkiewicz, P. K. and Rotunno, R.	1989	Low Froude number flow past three-dimensional obstacles. Part I: Baroclinically generated lee vortices. *J. Atmos. Sci.*, **46,** 1154–1164
	1990	Low Froude number flow past three-dimensional obstacles. Part II: Upwind flow reversal zone. *J. Atmos. Sci.*, **47,** 1498–1511
Williams, R. T., Peng, M. S. and Zankofski, D. A.	1992	Effects of topography on fronts. *J. Atmos. Sci.*, **49,** 287–305